Development and Validation of a Bulk-Flow Model for Staggered Labyrinth Seals

Filippo Cangioli[1] , Giuseppe Vannini[2], Paolo Pennacchi[1(✉)] ,
Lorenzo Ciuchicchi[3], Leonardo Nettis[2], Steven Chatterton[1] ,
and Andrea Vania[1]

[1] Politecnico di Milano, Via La Masa 1, 20156 Milan, Italy
paolo.pennacchi@polimi.it
[2] Baker Hughes, a GE Company, Via Felice Matteucci 2, 50127 Florence, Italy
[3] Baker Hughes, a GE Company, 480 Allée Gustave Eiffel, Le Creusot, France

Abstract. As well known, the stability assessment of turbomachines is strongly related to internal sealing components. For instance, labyrinth seals are widely used in compressors, steam and gas turbines and pumps to control the clearance leakage between rotating and stationary parts, owing to their simplicity, reliability and tolerance to large thermal and pressure variations. Labyrinth seals working principle consists in reducing the leakage by imposing tortuous passages to the fluid that are effective on dissipating the kinetic energy of the fluid from high-pressure regions to low-pressure regions. Conversely, labyrinth seals could lead to dynamics issues. Therefore, an accurate estimation of their dynamic behavior is very important. In this paper, the experimental results of a long-staggered labyrinth seal will be presented. The results in terms of rotordynamic coefficients and leakage will be discussed as well as the critical assessment of the experimental measurements.

Eventually, the experimental data are compared to numerical results obtained with the new bulk-flow model (BFM) introduced in this paper.

Keywords: Rotordynamics · Staggered labyrinth seal · Bulk-flow

Nomenclature

a_{ri}, a_{si}	Length of the rotor and stator of the i-th cavity
A_i, A_{0i}	Unsteady and steady cross-sectional area of the i-th cavity
B	Step height
C_{eff}	Effective damping of the seal
c_{xx}, c_{yy}	Direct damping of the seal in the x and y-directions
c_{xy}, c_{yx}	Cross-coupled damping of the seal in the x and y-directions
C	Average direct damping of the seal
Dh_i, Dh_{0i}	Unsteady and steady hydraulic diameter of the i-th cavity
e	Absolute roughness of the rotor and stator surface
$F_x(t), F_y(t)$	Lateral forces acting on the rotor
h_i, h_{0i}	Unsteady and steady enthalpy of the i-th cavity
H_i	Perturbed clearance of the i-th cavity
k_{xx}, k_{yy}	Direct stiffness of the seal in the x and y-directions
k_{xy}, k_{yx}	Cross-coupled stiffness of the seal in the x and y-directions

k	Average cross-coupled stiffness of the seal
$\dot{m}_i, \dot{m}_{0i}$	Unsteady and steady mass flow rate in the i-th cavity
NJ	Number of teeth
P_i, P_{0i}	Unsteady and steady pressure in the i-th cavity
r_0	Radius of the circular orbit of the rotor
R	Rotor radius
R_i	Rotor radius in the tooth location
s_i	Clearance of the i-th cavity
t	time
V_i, V_{0i}	Unsteady and steady tangential velocity in the i-th cavity
W	Tooth width at the tip of the i-th cavity
$x(t), y(t)$	Rotor displacement in the lateral directions
$\dot{x}(t), \dot{y}(t)$	Velocity of the rotor displacement in the lateral directions
ε	Perturbation parameter
ϑ	Angular coordinate
μ	Kinematic viscosity of the fluid
ρ_i, ρ_{0i}	Unsteady and steady density in the i-th cavity
ς_i	Speed of sound of the fluid in the i-th cavity
τ_{si}, τ_{s0i}	Unsteady and steady stator shear stress in the i-th cavity
ω	Whirling speed of the orbit of the rotor
Ω	Rotational speed of the rotor

Abbreviations

BC	Boundary condition
BFM	Bulk-flow model
CFD	Computational fluid dynamics
HPSTR	High-pressure seal test-rig

1   Introduction

The current trend in the field of power generation is the reduction of rotor-to-seal clearances to match the requirements of power output, efficiency and operational life. Conversely, this design approach leads to stability issues [1]. Therefore, the prediction of labyrinth seals dynamics needs much more attention.

Labyrinth seal is a non-contact seal, composed of two or more teeth arranged in a manner able to impose a tortuous passage to the fluid. The working principle is based on reducing the fluid leakage by dissipating the kinetic energy of the fluid via sequential cavities that are defined by position of the teeth. The teeth can be located on the rotor, stator or both. Depending on the teeth location, various configurations can be defined: straight-through, staggered, slanted and stepped labyrinth seals. Straight-through configuration is the most common labyrinth seal used in real applications because it is the easiest to be manufactured. However, staggered seals are becoming popular because they can reduce the leakage on equal radial clearance with respect to the straight-through ones. Generally, staggered seals are widely used in steam turbines

whereas straight-through seals are used in high-pressure compressors that historically show instability issues and this is the reason why academic research are mainly focused on this configuration. For staggered seals, there are few analytical models and experimental data for the prediction of their stability or instability contribution [2, 3].

The fluid-dynamics within the cavities of labyrinth seals is definitively influenced by the teeth location. Furthermore, the angle at which the flow approaches each tooth is correlated to the coefficients of discharge and to the kinetic energy carry-over coefficient, which strongly influence the leakage.

The dynamic force, produced by the non-uniform pressure distribution within the seal, in the direction of the rotor displacement (direct force) can change the natural frequencies of the machine, whereas the force in the orthogonal direction of the rotor displacement (cross-coupled force) can influence the stability.

The influence of labyrinth seals on the machine stability is typically investigated by using the standard finite beam-element rotordynamic model [16]. The dynamic behavior of labyrinth seals is modeled by the linearized coefficients [4], the so-called rotordynamic coefficients, using stiffness and damping matrices as,

$$-\begin{pmatrix} F_x(t) \\ F_y(t) \end{pmatrix} = \begin{bmatrix} k_{xx}(\omega) & k_{xy}(\omega) \\ k_{yx}(\omega) & k_{yy}(\omega) \end{bmatrix} \begin{pmatrix} x(t) \\ y(t) \end{pmatrix} + \begin{bmatrix} c_{xx}(\omega) & c_{xy}(\omega) \\ c_{yx}(\omega) & c_{yy}(\omega) \end{bmatrix} \begin{pmatrix} \dot{x}(t) \\ \dot{y}(t) \end{pmatrix} \qquad (1)$$

The inertia contribution in gas labyrinth seals is negligible; hence, the mass matrix is generally not considered. Due to the axisymmetric geometry of labyrinth seals, the eight linearized rotordynamics coefficients can be reduced to four. The stiffness and damping matrices are re-arranged as,

$$-\begin{pmatrix} F_x(t) \\ F_y(t) \end{pmatrix} = \begin{bmatrix} K(\omega) & k(\omega) \\ -k(\omega) & K(\omega) \end{bmatrix} \begin{pmatrix} x(t) \\ y(t) \end{pmatrix} + \begin{bmatrix} C(\omega) & c(\omega) \\ -c(\omega) & C(\omega) \end{bmatrix} \begin{pmatrix} \dot{x}(t) \\ \dot{y}(t) \end{pmatrix} \qquad (2)$$

In the following, the dependence of stiffness and damping coefficients from the whirling speed ω will be omitted for simplicity. The cross coupled stiffness coefficient k and direct damping coefficient C are responsible of destabilizing forces. The resulting cross-coupled force is given by,

$$F_t = (C\omega - k)r_0 \qquad (3)$$

where r_0 is the radius of the orbit. The effective damping can be defined as,

$$C_{eff} = C - \frac{k}{\omega} \qquad (4)$$

Labyrinth seals contribute with destabilizing effects on the machine dynamics when the effective damping is negative. The effective stiffness is defined as:

$$K_{eff} = K + c\,\omega \qquad (5)$$

and it is related to the machine natural frequency. Usually, the effective stiffness of labyrinth seals is not considered for the dynamic behavior for the machine because its value is one order of magnitude lower than that of journal bearings [5, 6].

The first analytical model of labyrinth seals, containing the fundamental physical elements for a dynamic characterization was given by Iwatsubo [7]. The model, well known as the bulk-flow model, is based on one-control volume (1CV) for each cavity of the labyrinth seal. Bulk-flow quantities can be defined in each CV. The continuity and circumferential momentum equations are solved for each cavity. The leakage mass-flow rate can be estimated via empirical correlations. The turbulence is considered by estimating the friction factor between the fluid and wall boundaries. The governing equations are solved using the perturbation method. Initially, the steady-state problem (rotor centered with the seal) must be solved. Then, the solution of the perturbed problem (by imposing an orbit to the rotor) that is also truncated at the first order, can be estimated by imposing an analytical form solution. Finally, the dynamic forces can be estimated by integrating the pressure along the circumferential direction. The rotordynamic coefficients are calculated by knowing the radius of the rotor orbit.

The bulk-flow model (BFM) represents the most used calculation method applied for industrial design to calculate the seal rotordynamic coefficients because it is time efficient compared to Computational Fluid Dynamics (CFD) approaches. Moreover, the accuracy of CFD predictions is comparable to BFM predictions [8].

A new BFM has been introduced starting from the considerations made from the authors in [9] and the results shown by Moore in [10]. New boundary conditions (BCs) can be defined in the BFM. The authors' assumption has been also validated by dedicated CFD analysis.

In this paper, the authors present the experimental results for a staggered labyrinth seal tested using the high-pressure seal test-rig (HPSTR) owned by the authors' company. The test rig allows the characterization of labyrinth seals in high-pressure conditions. The main capabilities and the identification procedures of the test-rig are described in a previous paper of the same authors [11]. The results of an experimental campaign on a 14 tooth-on-stator straight-through labyrinth seal have been reported in [9, 12]. The comparison with the experimental data shows improvement in the prediction of the rotordynamic coefficients.

2   Bulk-Flow Model

The baseline structure of the BFM developed by the authors for staggered labyrinth seals is here described. The model is based on the 1CV BFM developed by the same authors in [9, 13, 14]. The substantial differences with respect to the BFM for straight-through labyrinth seals are given by the geometry of the CVs, the leakage correlation used to estimate the axial velocity and by the impact of the inlet and outlet regions on the calculation of the rotordynamic coefficients.

The most innovative contribution, with respect to the models available in the literature, is the perturbation of the pressure and circumferential velocity in the inlet and outlet regions, where, usually, they are considered equal to zero in common BFMs [4, 9].

Moore observed in [10] that the contribution of the upstream and downstream sections on the calculation of the rotordynamic coefficients is not negligible. He proposed a 3D-CFD model to predict the flow conditions and rotordynamic coefficients. By considering the inlet and outlet regions for the estimation of the fluid forces on the rotor, the predictions become more accurate compared to experimental results. Because the seal force is generated by the perturbation of the pressure, the assumption of null perturbation of the pressure in the inlet and outlet regions is not correct.

In the model proposed in this paper, two additional CVs have been added at the inlet and outlet regions with a proper mathematical treatment of the governing equations.

2.1 Governing Equations

The governing equations are represented by the continuity, circumferential momentum and energy equations. The energy equation is evaluated only in the zeroth-order problem as described in [13]. 1CV for each cavity has been considered as shown in Fig. 1.
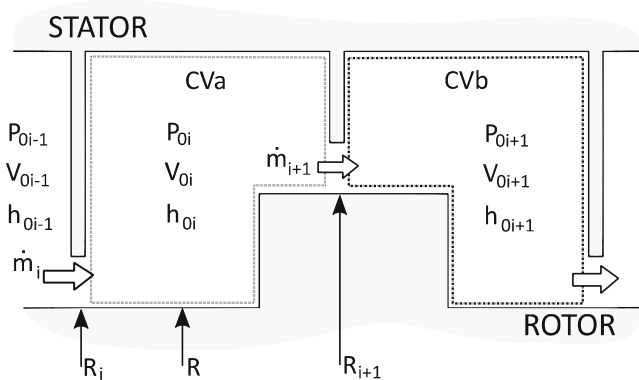

Fig. 1. CVs and bulk-flow quantities.

Because long teeth alternate with the rotor steps, two different CVs can be defined. The control volume labelled as CVa in Fig. 1, presents the long tooth on the upstream side and the short tooth combined with the rotor step on the downstream side. The control volume labelled as CVb in Fig. 1, presents the short tooth combined with the rotor step on the upstream side and the long tooth on the downstream side. Because the enthalpy is assumed to be independent on the orbit motion of the rotor as explained in [9], the derivatives of the enthalpy with respect to the time and to the angular coordinate are null. The governing equations can be stated as,

- Continuity equation:

$$\frac{\partial}{\partial t}(\rho_i A_i) + \frac{\partial}{\partial \vartheta}\left(\frac{\rho_i A_i V_i}{R}\right) + \dot{m}_{i+1} - \dot{m}_i = 0 \tag{6}$$
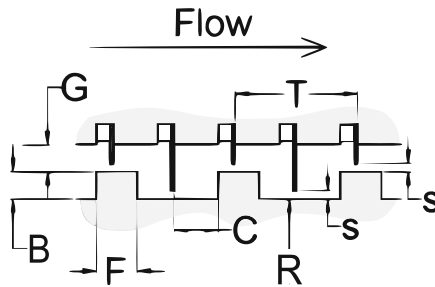
- Circumferential momentum equation:

$$\frac{\partial}{\partial t}(\rho_i A_i V_i) + \frac{\partial}{\partial \vartheta}\left(\frac{\rho_i A_i V_i^2}{R}\right) + \dot{m}_{i+1}V_i - \dot{m}_i V_{i-1} = -\frac{A_i}{R}\frac{\partial P_i}{\partial \vartheta} + \tau_{ri}a_{ri} - \tau_{si}a_{si} \tag{7}$$

- Energy equation:

$$\dot{m}_i\left(h_i + \frac{V_i^2}{2}\right) - \dot{m}_{i+1}\left(h_{i-1} + \frac{V_{i-1}^2}{2}\right) = \tau_{ri}a_{ri}R\Omega \tag{8}$$

where P_i, V_i, ρ_i and h_i are the bulk-flow pressure, the circumferential velocity, the density and the enthalpy in the i-th cavity of the seal respectively.

Fig. 2. Scheme and nomenclature used to describe staggered labyrinth seals.

The geometrical quantities A_i, a_{ri} and a_{si} represent the tangential area and the dimensional lengths where the shear stresses are applied. The tangential area has different expressions depending on the type of CV considered.

Using the nomenclature given in Fig. 2, the tangential area for CVa and CVb, is defined, respectively, as

$$A_i = \left(\frac{T}{2} - W\right)(B + G) - \left(\frac{T}{2} - W - C\right)B \tag{9}$$

and

$$A_i = \left(\frac{T}{2} - W\right)(B + G) - \left(C + F - \frac{T}{2}\right)B \tag{10}$$

whereas, a_{ri} and a_{si} are defined for both the CVs as,

$$a_{ri} = \frac{T}{2} - W + B \tag{11}$$

$$a_{si} = \frac{T}{2} - W + 2(G - s) + B \tag{12}$$

The leakage correlation replaces the axial momentum equation in defining the axial velocity and pressure distributions along the seal cavities. The leakage correlation employed in the model is the generalized Neumann correlation for real gases [15]:

$$\dot{m}_i = \frac{R_i}{R} C_{fi} H_i \sqrt{P_{i-1}\rho_{i-1} - P_i\rho_i} \tag{13}$$

where C_{fi} is the discharge coefficients and H_i is the dynamic radial clearance. The leakage is per unit circumferential length because the governing equations are divided by $2\pi R$. The axial cross-sectional area for the leakage (annulus area) is equal, for the CVa, to $\pi(R + H_i)^2 - \pi R^2$ that can be approximated to $2\pi R H_i$. Thus, dividing the leakage by $2\pi R$, only the term H_i remains in the leakage equation. Thus, for the CVa control volume, $\frac{R_i}{R} = 1$ and $\frac{R_i}{R} = 1 + \frac{H_i}{R}$ for the CVb control volume.

In staggered labyrinth seals, the kinetic energy carry-over coefficient is equal to the unity for all the teeth as suggested by Childs [5]. The discharge coefficient has been estimated by the Chaplygin correlation as,

$$C_{fi} = \frac{\pi}{\pi + 2 - 5s_{0i} + 2s_{0i}^2}$$
$$s_{0i} = \left(\frac{P_{i-1}}{P_i}\right)^{\frac{\gamma-1}{\gamma}} - 1 \tag{14}$$

If the flow sonic condition is reached under the last tooth (choked flow), the leakage mass flow-rate becomes independent by the downstream pressure. To check if the flow is subsonic or choked, the axial velocity is compared with the speed of sound (ς) of the fluid. The speed of sound is evaluated using the fluid properties database and it is a function of the pressure and density of the previous cavity ($\varsigma_i = f(P_{i-1}, \rho_{i-1})$).

The axial velocity is estimated using the definition of the leakage mass flow-rate, which is:

$$U_i = \frac{\dot{m}_i}{C_{fi} H_i \rho_{i-1}} \tag{15}$$

If the axial velocity is equal or larger than the speed of sound, the leakage mass-flow rate equation becomes:

$$\dot{m}_i = C_{fi} H_i \rho_{i-1} \varsigma_i \tag{16}$$

For the calculations of the circumferential shear stresses (τ_{si} on the stator and τ_{ri} on the rotor), it is necessary to use a correlation explicit formula to estimate the Darcy friction factor (f_{si} and f_{ri}). The shear stresses are defined as:

$$\tau_{si} = \frac{\rho_i}{2} f_{si} V_i V_{Si} \tag{17}$$

$$\tau_{ri} = \frac{\rho_i}{2} f_{ri} (R\Omega - V_i) V_{Ri} \tag{18}$$

where V_{Si} and V_{Ri} are the modulus of the fluid velocity, on the stator and rotor surfaces respectively, considering the axial and circumferential components of the velocity. They can be defined as:

$$V_{Si} = \sqrt{U_i^2 + V_i^2} \tag{19}$$

$$V_{Ri} = \sqrt{U_i^2 + (R\Omega - V_i)^2} \tag{20}$$

For the calculation of the circumferential shear stresses, the Swamee-Jain correlation is used to estimate the friction factor between the fluid and the rotor/stator wall, as described in [13].

2.2   Perturbation Analysis

The perturbation analysis is used to solve the continuity and circumferential momentum equations. The rotor position is perturbed with respect to the centred position, and a circular orbit is assumed.

$$P_i = P_{0i} + \varepsilon P_{1i}(t, \vartheta) \tag{21}$$

$$\rho_i = \rho_{0i} + \varepsilon \rho_{1i}(t, \vartheta) \tag{22}$$

$$h_i = h_{0i} \tag{23}$$

$$V_i = V_{0i} + \varepsilon V_{1i}(t, \vartheta) \tag{24}$$

$$H_i = s_i + \varepsilon H_1(t, \vartheta) \tag{25}$$

The perturbation theory comprises mathematical methods for finding an approximate solution of the problem, by starting from the steady-state solution (centred rotor within the seal). The solutions of the problem are expanded and truncated at the first-order, hence the thermodynamic and kinematic variables of the model (generally indicated with the symbol $\square$) are separated in the steady-state terms $\square_{0i}$ and in the perturbed terms $\square_{1i}(t, \vartheta)$.

2.3   Zeroth-Order Problem

The continuity, circumferential momentum and energy zeroth-order equations, for each CV in the seal cavities, are iteratively solved using the multi-variate Newton-Raphson algorithm to find the solution in terms of pressure, density, enthalpy and circumferential velocity in each cavity. The boundary conditions (BCs) used in the zeroth-order problem are the Dirichlet BCs in the inlet and outlet sides. The inlet pressure, circumferential velocity and enthalpy are imposed at the inlet, whereas the outlet pressure, circumferential velocity and enthalpy are imposed at the outlet side. These quantities are calculated by using the seal operating conditions: inlet/static pressure, inlet temperature, pre-swirl and rotor rotational speed. The solution of the zeroth-order problem must satisfy the following equations:

$$\dot{m}_{01} \equiv \cdots \equiv \dot{m}_{0i} \equiv \cdots \equiv \dot{m}_{0NT} \equiv \dot{m}_0 \tag{26}$$

$$\dot{m}_0 V_{0i} - \dot{m}_0 V_{0i-1} = \tau_{0ri} a_{ri} - \tau_{0si} a_{ri} \tag{27}$$

$$\dot{m}_0 \left(h_{0i} + \frac{V_{0i}^2}{2} \right) - \dot{m}_0 \left(h_{0i-1} + \frac{V_{0i-1}^2}{2} \right) = \tau_{0ri} a_{ri} R\Omega \tag{28}$$

The main contribution of the energy equation is the coupling of the continuity equation with the circumferential momentum equation in the zeroth-order problem. Considering an isenthalpic process, these equations are independent one from each other, and the estimation of the mass flow-rate and thermodynamic properties of the fluid (steady pressure and density) does not depend on the circumferential velocity. In the model developed in this paper, the equations are linked because the density depends on the enthalpy that is calculated (in the energy equation) based on the circumferential velocity and rotor shear stress.

2.4   First-Order Problem

The first-order problem is governed by the continuity and circumferential momentum equations. By imposing a circular orbit to the rotor and linearizing the governing equations, the only solutions admitted for the perturbed pressure and circumferential velocity have the same mathematical expression of the perturbed clearance.

By imposing them, the first-order equations result as,

- Continuity first-order equation:

$$
\begin{aligned}
&\frac{A_{0i} \frac{\partial \rho_i}{\partial P_{1i}} V_{0i}}{R} \frac{\partial P_{1i}}{\partial \vartheta} + A_{0i} \frac{\partial \rho_i}{\partial P_{1i}} \frac{\partial P_{1i}}{\partial t} + \frac{A_{0i} \rho_i}{R} \frac{\partial V_{1i}}{\partial \vartheta} \\
&+ \left(\frac{\partial \dot{m}_{i+1}}{\partial P_{1i}} - \frac{\partial \dot{m}_i}{\partial P_{1i}} \right) P_{1i} - \frac{\partial \dot{m}_i}{\partial P_{1i-1}} P_{1i-1} \\
&+ \frac{\partial \dot{m}_{i+1}}{\partial P_{1i+1}} P_{1i+1} = -\frac{\left(\frac{T}{2} - W \right) \rho_i V_{0i}}{R} \frac{\partial H_1}{\partial \vartheta} \\
&- \left(\frac{T}{2} - W \right) \rho_i \frac{\partial H_1}{\partial t} - \left(\frac{\partial \dot{m}_{i+1}}{\partial H_1} - \frac{\partial \dot{m}_i}{\partial H_1} \right) H_1
\end{aligned}
\tag{29}
$$

- Circumferential momentum first-order equation:

$$\frac{\left(\frac{T}{2}-W\right)\rho_i V_{0i}^2}{R}\frac{\partial H_1}{\partial \vartheta} + \left(\frac{A_{0i}}{R} + \frac{A_{0i} V_{0i}^2}{R}\frac{\partial \rho_i}{\partial P_{1i}}\right)\frac{\partial P_{1i}}{\partial \vartheta} + \frac{2A_{0i}\rho_i V_{0i}}{R}\frac{\partial V_{1i}}{\partial \vartheta}$$
$$+ A_{0i}\rho_i\frac{\partial V_{1i}}{\partial t} + \left(\frac{T}{2}-W\right)\rho_i V_{0i}\frac{\partial H_1}{\partial t}$$
$$+ H_1\left(-a_{ri}\frac{\partial \tau_{rli}}{\partial H_1} + a_{si}\frac{\partial \tau_{sli}}{\partial H_1} + \frac{\partial \dot{m}_i}{\partial H_1}(V_{0i} - V_{0i-1})\right)$$
$$+ V_{1i}\left(-a_{ri}\frac{\partial \tau_{rli}}{\partial V_{1i}} + a_{si}\frac{\partial \tau_{sli}}{\partial V_{1i}} + \dot{m}_0\right) \tag{30}$$
$$+ P_{1i-1}\left(\frac{\partial \tau_{rli}}{\partial P_{1i-1}}(a_{si} - a_{ri}) + \frac{\partial \dot{m}_i}{\partial P_{1i-1}}(V_{0i} - V_{0i-1})\right)$$
$$+ P_{1i}\left(\frac{\partial \tau_{rli}}{\partial P_{1i}}(a_{si} - a_{ri}) + \frac{\partial \dot{m}_i}{\partial P_{1i}}V_{0i-1} - \frac{\partial \dot{m}_{i-1}}{\partial P_{1i}}V_{0i}\right) + A_{0i}V_{0i}\frac{\partial \rho_i}{\partial P_{1i}}\frac{\partial P_{1i}}{\partial t}$$
$$+ \frac{\partial \dot{m}_{i+1}}{\partial P_{1i+1}}V_{0i}P_{1i+1} - \dot{m}_0 V_{1i-1} - \dot{m}_0 V_{1i-1} + \frac{\partial \dot{m}_i}{\partial P_{1i-1}}(V_{0i} - V_{0i-1})P_{1i-1} = 0$$

Generally, the perturbation of the pressure and circumferential velocity at the inlet and outlet regions are assumed to be equal to zero.

As already said, a novelty has been introduced in the model proposed in this paper by considering the perturbation of the pressure and circumferential velocity in the inlet and outlet regions. Two additional CVs, one in the inlet and one in the outlet region, have been introduced in the seal model. Consequently, the first-order continuity and circumferential momentum equations are solved also in the additional CVs. Nevertheless, the zeroth-order solution for these CVs is required, as well as the BCs for the zeroth-order problem. It is reasonable to assume that the zeroth-order upstream pressure with respect to the inlet region (P_{0ui}) is the same of the inlet (P_{0in}).
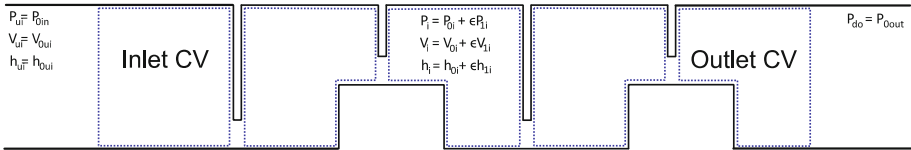

Fig. 3. Control volumes used in the BFM proposed by the authors.

The same assumption is made for the zeroth-order downstream pressure with respect to the outlet region (P_{0do}) that is equal to the outlet pressure (P_{out}). The zeroth-order circumferential velocities (V_{0ui}, V_{0do}) and enthalpies (h_{0ui}, h_{0do}) can be calculated using the zeroth-order circumferential momentum and energy equations.

Regarding the BCs for the first-order problem, it can be reasonably assumed that the perturbed pressures (P_{1ui}, P_{1do}) and circumferential velocities (V_{1ui}, V_{1do}) at the seal CVs boundaries can be considered null sufficiently far from the seal cavities. The scheme of the BCs is reported in Fig. 3. Because the perturbed pressure in the upstream inlet region is null and the steady-state pressure is equal to that of the inlet region ($P_{ui} = P_{0in}$), the mass-flow rate between these two CVs cannot be expressed using the Neumann correlation (see Eq. (13)). However, a leakage exists, and it is assumed to be equal to the steady-state mass-flow ($\dot{m}_0$) and independent on the perturbation of the

inlet region. Therefore, by considering the continuity and circumferential momentum equations for the Inlet CV, the derivatives of the incoming mass-flow with respect to the perturbed pressures P_{1in} and P_{1ui} are equal to zero. Consequently, the following terms are null in the first-order equations:

$$\frac{\partial \dot{m}_{in}}{\partial P_{1in}} = 0 \tag{31}$$

$$\frac{\partial \dot{m}_i}{\partial P_{1ui}} = 0 \tag{32}$$

For the same reasons, by considering the continuity and circumferential momentum equations in the Outlet CV, the derivatives of the outgoing mass-flow with respect to the perturbed pressure are equal to zero. Consequently, the following the terms are null in the first-order equations:

$$\frac{\partial \dot{m}_{out+1}}{\partial P_{1out}} = 0 \tag{33}$$

$$\frac{\partial \dot{m}_{out+1}}{\partial P_{1do}} = 0 \tag{34}$$

As previously stated, Moore in [10] demonstrated that the upstream and downstream sections contribute to the rotordynamic coefficients. By comparing the CFD results with experimental measurements, the introduction of inlet and outlet regions, improved the CFD predictions [17]. In this paper, the authors performed a CFD analysis based on the Integral Perturbation Method (IPM) aimed at estimating the perturbation of the pressure in the inlet region and to prove the assumptions made in the BFM. The IPM considers the full unsteady simulation with the mesh motion to directly consider rotor oscillatory movements. The CFD analysis clearly shows that the contribution of the inlet and outlet regions to the dynamic forces, generated by the surrounding fluid, is not negligible. This fact conflicts with the assumption in the original BFM in which the perturbation of the pressure is considered null at the inlet and outlet regions.

2.5   Calculation of the Rotordynamic Coefficients

The dynamic force acting on the rotor [9] surrounded by the labyrinth seal is given by:

$$F = F_x + \mathrm{j}F_y = -\varepsilon R_s \sum_{i=1}^{N-1} L_i \left[\int_0^{2\pi} \left(P_{1i}\mathrm{e}^{\mathrm{j}\vartheta} - \mathrm{j}a_{ri}\tau_{r1i}P_{1i}\mathrm{e}^{\mathrm{j}\vartheta} \right) \right] \tag{35}$$

The solution of the two equations obtained by considering the real and imaginary parts of Eq. (35) allows the rotordynamic coefficients to be defined as:

$$K = \tfrac{1}{2}\mathrm{Re}(Z^+ + Z^-) \quad k = -\tfrac{1}{2}\mathrm{Im}(Z^+ + Z^-) \tag{36}$$

$$C = -\tfrac{1}{2\Omega}\mathrm{Im}(Z^+ - Z^-) \quad c = -\tfrac{1}{2\Omega}\mathrm{Re}(Z^+ - Z^-) \tag{37}$$

where,

$$Z^+ = \pi R_s \sum_{i=1}^{N-1}\left(\frac{T}{2} - W\right)\int_0^{2\pi}\left[P_{1i}^+\left(1 - \mathrm{j}a_{ri}\frac{\partial\tau_{ri}}{\partial P_{1i}}\right) - \mathrm{j}a_{ri}\frac{\partial\tau_{ri}}{\partial V_{1i}}V_{1i}^+ + \mathrm{j}a_{ri}\frac{\partial\tau_{ri}}{\partial H_1}\right] \tag{38}$$

$$Z^- = \pi R_s \sum_{i=1}^{N-1}\left(\frac{T}{2} - W\right)\int_0^{2\pi}\left[P_{1i}^-\left(1 - \mathrm{j}a_{ri}\frac{\partial\tau_{ri}}{\partial P_{1i}}\right) - \mathrm{j}a_{ri}\frac{\partial\tau_{ri}}{\partial V_{1i}}V_{1i}^- + \mathrm{j}a_{ri}\frac{\partial\tau_{ri}}{\partial H_1}\right] \tag{39}$$

Each cavity contributes to the overall rotordynamic coefficients. The sum of the rotordynamic coefficient of each cavity allows the coefficients of the seal to be obtained.

3   Experimental Campaign

The main features of the HPSTR are [11]:

- inlet pressure up to 500 bar;
- pressure ratio up to 2.5;
- rotational speed up to 15000 rpm;
- control of the rotor orbit by active magnetic bearings (AMBs) with an excitation frequency up to 250 Hz;
- multiple excitation frequencies;
- interchangeable swirler device to set the desired pre-swirl ratio (also negative pre-swirl ratio by inverting the rotational speed);
- possibility to test off-center rotor position.

Figure 4 shows the external casing of the HPSTR that is very similar to an actual industrial plant because it is equipped with a high-pressure compressor, a gearbox and an electric motor connected to a complex high-pressure gas loop. All these details are not provided here because already illustrated in [11].

The HPSTR working principle consists of injecting the nitrogen into the casing at controlled pressure. The gas flows through the swirler device which sets the circumferential velocity of the fluid and the pre-swirl at the seal entrance. Then, the nitrogen flows into the two test seals that are the object of the test. Their back-to-back configuration is used to balance the axial load. The orbit motion of the rotor is controlled by AMBs, which apply the needed dynamic forces to shake the rotor. These forces are measured through current measurements and dedicated calibrations, see [11].

The rotordynamic coefficients associated to the labyrinth seals are finally computed applying an identification algorithm which is based on simple rotor equations of
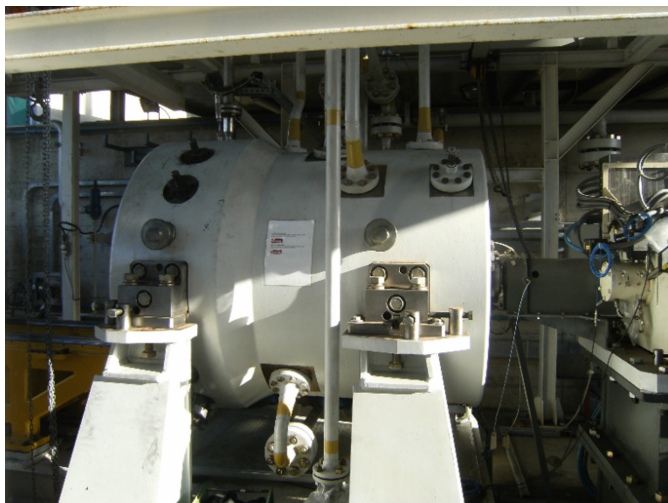
Fig. 4. High-pressure seal test-rig.

motion. All relevant forces and displacements are measured and equations are inverted solving for the unknown coefficients. With respect to the experimental activity described in [12], the instrumentation has been improved by introducing a specific probe to measure more precisely the pre-swirl at the seal entrance. An accurate measurement of process parameters is critical to compare the experimental tests data to predictions.
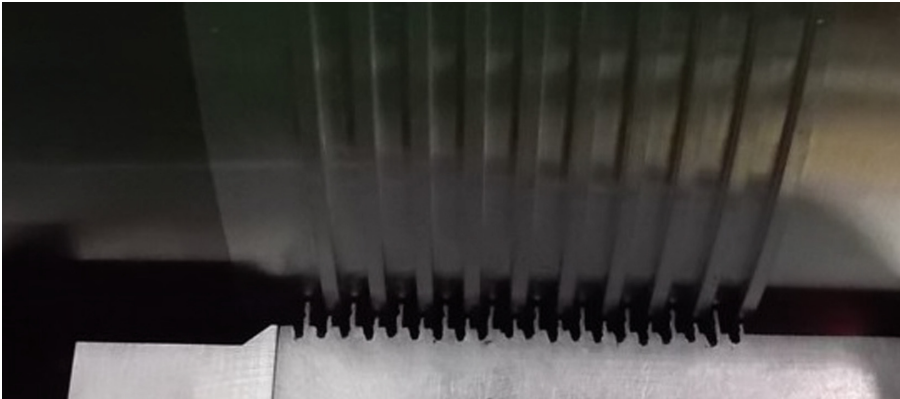
The staggered labyrinth seal tested in the HPSTR is representative of a balancing drum seal mounted in a medium steam turbine (see Fig. 5). The final layout of the staggered labyrinth seals is shown in Fig. 6. The geometrical parameters of the labyrinth seal and operating conditions are listed in Table 1.
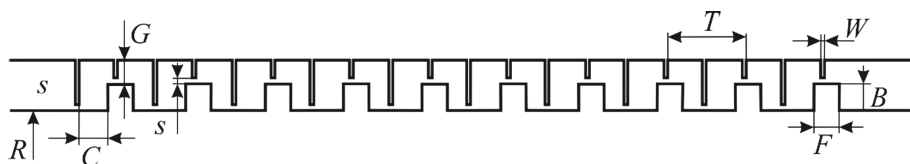
Fig. 5. Scheme of the staggered labyrinth seal used in the experimental tests.

The radial clearance listed in Table 1 is the nominal one, therefore it doesn't consider the radial growth caused by the centrifugal force. For confidential reasons, only two experiments are shown in the paper.

The experimental data in terms of rotordynamic coefficients and leakage mass-flow are shown, compared to the numerical predictions, in the body of the paper and in the Appendix A.

Fig. 6. Final layout of the staggered labyrinth seal installed in the HPSTR.

Table 1. Seal geometry and operating conditions.

Geometry		
Shaft radius (R)	110	mm
Nominal radial clearance (s)	0.50	mm
Steps-to-casing radial distance (G)	2.00	mm
Steps height (B)	2.00	mm
Steps width (F)	2.00	mm
J-strips width at tip (W)	0.30	mm
J-strips pitch (T)	3.00	mm
J-strip-to-step axial distance (C)	2.20	mm
J-strips number	20	
Rotor steps number	10	
Rotor/stator roughness	3.2	μm
Operating conditions	Exp. A	Exp. B
Inlet pressure (bar) P_{in}	64.57	91.94
Outlet pressure (bar) P_{out}	46.38	70.41
Pressure ratio	1.39	1,30
Inlet temperature (°C)	31.46	21.13
Pre-swirl ratio	0.36	0.34
Rotational speed (rpm) Ω	12000	12000
Whirling speeds (rpm) ω	4200, 5880, 7560, 9240, 10920	4200, 5880, 7560, 9240, 10920

4   Comparison with Experimental Data and Numerical Results

The numerical results, in terms of rotordynamic coefficients and leakage mass-flow, have been compared with the experimental measurements.

The direct damping and cross-coupled stiffness are shown in Figs. 7 and 8, where the numerical results of the original BFM and those considering also the inlet and outlet regions are also plotted. The BFM with the inlet and outlet regions takes into account for the rotordynamic coefficients generated in the two "new" CVs. By considering only the CVs in the cavities of the seal, and taking into account the perturbation of the pressure and circumferential velocity at the seal boundaries, a new BFM can be introduced. The new BFM considers different BCs with respect to the original one. Thus, three different models are shown in the following paper.

It can be noticed in Figs. 7 and 8 that both the BFM with the inlet and outlet regions and the BFM with new BCs are more accurate in the estimation of the rotordynamic coefficients than the original BFM. Slight differences can be observed between the two new BFMs. It can be deduced that the assumption of considering the perturbation of the pressure and circumferential velocity at the seal boundaries equal to zero is not correct if compared to CFD result as already noticed by Moore. Moreover, the predictions of the rotordynamic coefficients is strongly improved.

The uncertainty range for each measured point is also reported. The uncertainties are larger with the increase in the whirling speed. The trends of the two experiments are very similar. As expected, the coefficients are frequency dependent as already shown for a teeth-on-stator straight-through labyrinth seal in [12]. The experimental coefficients of the experiment B are higher than those of the experiment A because of the higher pressure drop condition.
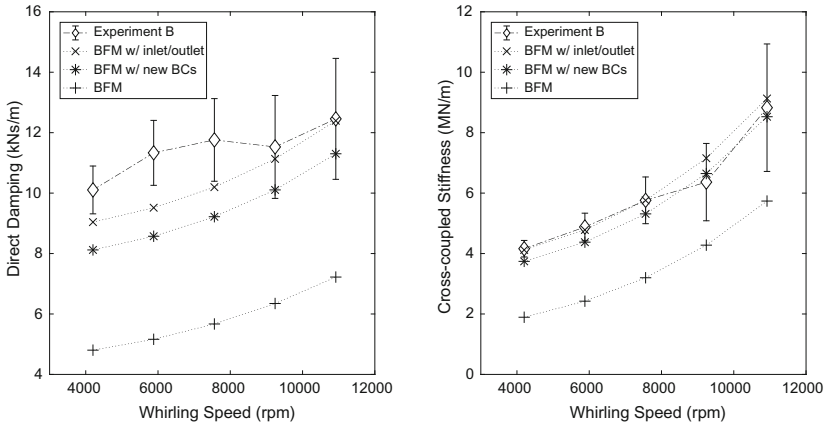
Generally, the trend of the coefficients as a function of the whirling speed is well reproduced by the three BFMs. The direct damping is slightly underestimated with respect to the experimental one. Thus, BFMs result to be conservative in the rotordynamic design phase.

The comparison of the mass-flow measured during the experiments with those predicted by the bulk-flow model for both experiments is shown in Fig. 9. The uncertainty range is almost 10% of the average value. The predictions are very accurate compared to the experimental measurements. The mass-flow is the same for the BFMs considered in the paper.

The contribution of each cavity of the seal to the rotordynamic coefficients is shown in Fig. 10. The solid lines are the results of the original BFM, whereas the dotted lines are the results of the model by considering the perturbation in the inlet and outlet regions. Five lines for each model are represented in the Fig. 10, consistently with the five whirling frequencies.
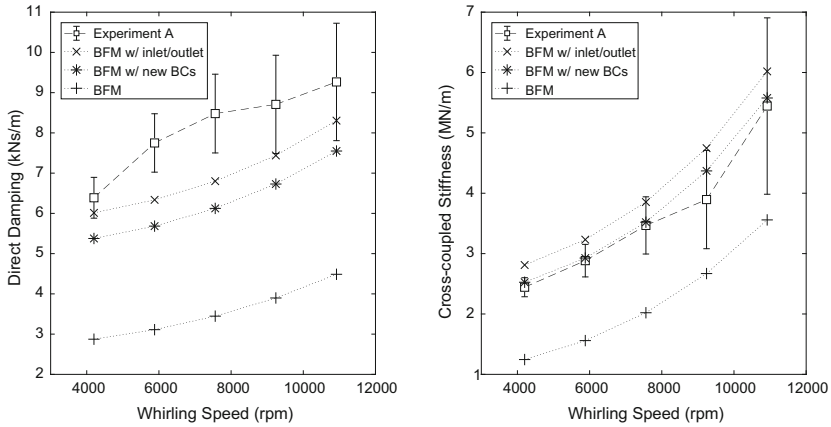
Fig. 7. Comparison of predictions and measurements of direct damping and cross-coupled stiffness coefficients as a function of the whirling speed for the experiment A.

Fig. 8. Comparison of predictions and measurements of direct damping and cross-coupled stiffness coefficients as a function of the whirling speed for the experiment B.

It can be observed that the new BFMs show a different trend of the coefficients. In the original BFM seems that the coefficients in the first and last cavities are constrained to be close to zero by the fact that the perturbations are null at the boundaries.

Despite the perturbations are considered both in the inlet and outlet in the new BFM, the coefficients at the seal end are equal to the coefficients calculated with the original BFM. Trying to figure out a correlation between the coefficients and the zeroth-order quantities, the trend of the coefficients of the new BFM is similar to that of the zeroth-order pressure and density along the seal cavity. Whereas, the coefficients calculated with the original BFM are uncorrelated with all the zeroth-order quantities.

By considering the results in Figs. 7 and 8 for the experiment B, the BFM with the inlet and outlet regions consider the coefficients contribution of the inlet and outlet cavities as shown in Fig. 10.
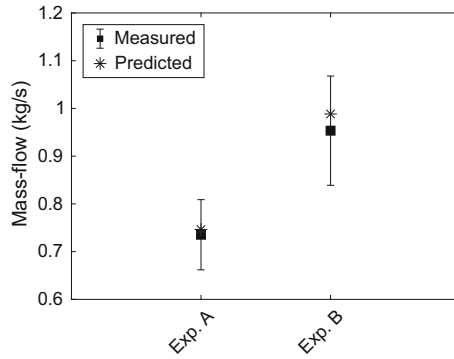
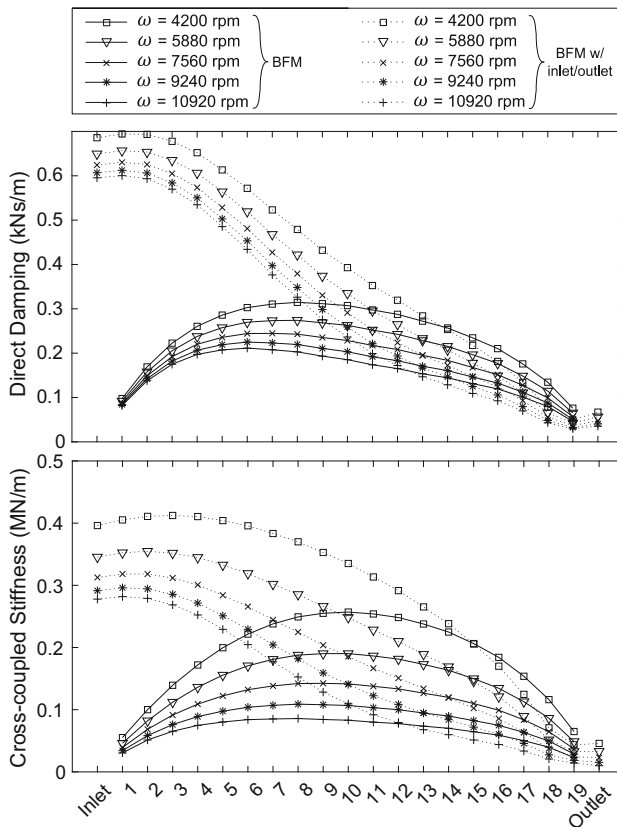**Fig. 9.** Comparison of the mass-flow measured and predicted.

Fig. 10. Trend of the predicted direct damping and cross-coupled stiffness as a function of the seal's cavity for the experiment B.

The BFM with new BCs considers the coefficients of the model with the inlet and outlet regions but the overall seal coefficients do not take into account the coefficient contributions of the inlet and outlet regions, but only those corresponding to the cavities from 1 to 19 (see Fig. 10), such as for the original BFM.

This approach is finally making the BFM physically more consistent and improves the match with experimental data by an average factor 2 which is not negligible at all.

5 Conclusion

In the paper, the experimental results obtained from an experimental campaign on a staggered labyrinth seal have been presented and a new BFM has been introduced by considering the perturbation of the pressure and circumferential velocity in the inlet and outlet regions.

Actual BFMs consider the perturbations null despite perturbations are captured by Moore comparing CFD analysis with experimental measurements. The new BFMs improve the predictions of the rotordynamic coefficients compared to experiments by an average factor 2. The predicted mass-flow are very accurate for both the tests. he baseline structure of the BFM developed by the authors for staggered labyrinth seals is here described. The model is based on the 1CV BFM developed by the same authors in [9, 13, 14]. The substantial differences with respect to the BFM for straight-through labyrinth.

Appendix A

The experimental measurements and numerical predictions of the direct stiffness and cross-coupled damping coefficients are reported here for both the experiments. Additionally, the effective stiffness coefficients is shown (Figs. 11, 12 and 13).
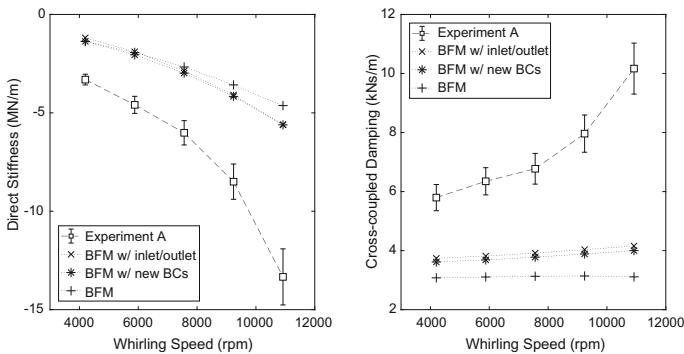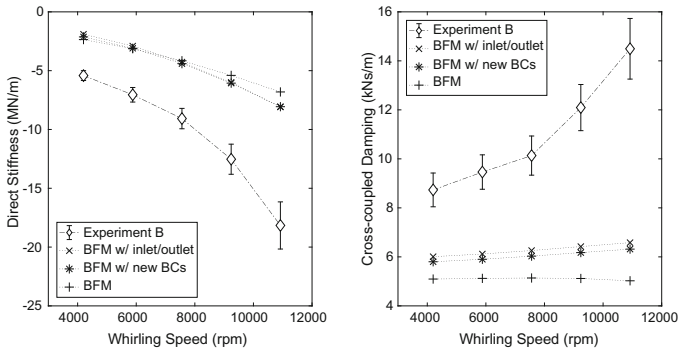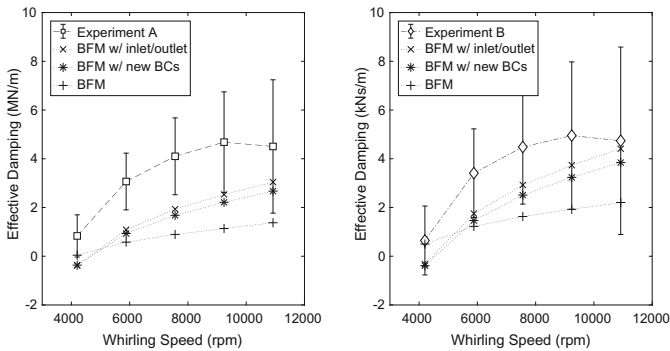

Fig. 11. Comparison of predictions and measurements of direct stiffness and cross-coupled damping coefficients as a function of the whirling speed for the experiment A.

Fig. 12. Comparison of predictions and measurements of direct stiffness and cross-coupled damping coefficients as a function of the whirling speed for the experiment B.

Fig. 13. Comparison of predictions and measurements of the effective damping coefficient as a function of the whirling speed for the experiment A and B.

References

1. Cangioli, F., Pennacchi, P., Vania, A., Chatterton, S., Dang, P.V.: Analysis of the dynamic behavior of two high-pressure turbines for the detection of possible rub symptoms. In: Proceedings of ASME Turbo Expo 2016: Turbomachinery Technical Conference and Exposition, Seoul, South Korea (2016). https://doi.org/10.1115/gt2016-56627
2. Kirk, R.: Labyrinth seal analysis for centrifugal compressor design—theory and practice. In: Second IFToMM International Conference on Rotordynamics, Tokyo (1986)
3. Wagner, N.G.: Reliable rotor dynamic design of high-pressure compressors based on test rig data. J. Eng. Gas Turbines Power **123**(4), 849–856 (2000)
4. Childs, D.W., Scharrer, J.K.: An Iwatsubo-based solution for labyrinth seals: comparison to experimental results. J. Eng. Gas Turbines Power **108**, 325–331 (1986)
5. Dang, P., Chatterton, S., Pennacchi, P., Vania, A., Cangioli, F.: An experimental study of nonlinear oil-film forces in a tilting-pad journal bearing. In: ASME Conference, Boston, USA (2015)

6. Dang, P., Chatterton, S., Pennacchi, P., Vania, A., Cangioli, F.: Investigation of load direction on a five-pad tilting pad journal bearing with variable clearance. In: Proceedings of the 14th IFToMM World Congress, Taipei, Taiwan (2015)

7. Iwatsubo, T.: Evaluation of instability forces of labyrinth seals in turbines or compressors. In: NASA CP 2133, Proceedings of a Workshop at Texas A&M University, Rotordynamic Instability Problems in High Performance Turbomachinery, pp. 205–222 (1980)

8. Sreedharan, S., Vannini, G., Mistry, H.: CFD assessment of rotordynamic coefficients in labyrinth seals. In: ASME Turbo Expo 2014: Turbine Technical Conference and Exposition, Düsseldorf, Germany (2014)

9. Cangioli, F., Pennacchi, P., Vannini, G., Ciuchicchi, L.: Effect of energy equation in one control-volume bulk-flow model for the prediction of labyrinth seal dynamic coefficients. Mech. Syst. Signal Process. **98**, 594–612 (2018)

10. Moore, J.J.: Three-dimensional CFD rotordynamic analysis of gas labyrinth seals. J. Vib. Acoust. **125**(4), 427–433 (2003)

11. Vannini, G., Cioncolini, S., Calicchio, V., Tedone, F.: Development of a high pressure test rig for centrifugal compressors internal seals characterization. In: Proceedings of the Fortieth Turbomachinery Symposium, vol. %1 di %2 Houston, Texas, 12–15 September 2011

12. Vannini, G., Cioncolini, S., Del Vescovo, G., Rovini, M.: Labyrinth seal and pocket damper seal high pressure rotordynamic test data. J. Eng. Gas Turbines Power **136**(2), 022501 (2014)

13. Cangioli, F., Pennacchi, P., Vannini, G., Ciuchicchi, L., Vania, A., Chatterton, S., Dang, P. V.: On the thermodynamic process in the bulk-flow model for the estimation of the dynamic coefficients of labyrinth seals. J. Eng. Gas Turbines Power (2017). https://doi.org/10.1115/1.4037919

14. Cangioli, F., Chatterton, S., Pennacchi, P., Nettis, L., Ciuchicchi, L.: Thermo-elasto bulk-flow model for labyrinth seals in steam turbines. Tribol. Int. **119**, 359–371 (2018)

15. Cangioli, F., Pennacchi, P., Riboni, G., Vannini, G., Ciuchicchi, L., Vania, A., Chatterton, S.: Sensitivity analysis of the one-control volume bulk-flow model for a 14 teeth-on-stator straight-through labyrinth seal. In: Proceedings of ASME Turbo Expo 2017: Turbomachinery Technical Conference and Exposition, Charlotte, NC (2017). https://doi.org/10.1115/gt2017-63014

16. Lalanne, M., Ferraris, G.: Rotordynamics Predictions in Engineering. Wiley, Chichester (1998)

17. Cangioli, F., Pennacchi, P., Nettis, L., Ciuchicchi, L.: Design and analysis of CFD experiments for the development of bulk-flow model for staggered labyrinth seal. Int. J. Rotating Mach. **2018**, 1–16 (2018). Article no. 9357249